

Kinetic Modeling of CO_{ad} Monolayer Oxidation on Carbon-Supported Platinum Nanoparticles

Bernhard Andreus,^{†,‡} Frédéric Maillard,[§] Joanna Kocylo,^{†,‡} Elena R. Savinova,^{||} and Michael Eikerling^{*,†,‡}

Department of Chemistry, Simon Fraser University, 8888 University Drive, Burnaby, British Columbia V5A 1S6, Canada, Institute for Fuel Cell Innovation, National Research Council Canada, 4250 Wesbrook Mall, Vancouver, British Columbia V6T 1W5, Canada, Laboratoire d'Electrochimie et de Physico-chimie des Matériaux et des Interfaces, UMR 5631 CNRS/INPG/UJF, 1130 Rue de la Piscine, BP75, 38402 Saint Martin d'Hères, France, and Boreskov Institute of Catalysis, Pr. Akademika Lavrentieva 5, 630090 Novosibirsk, Russia

Received: June 20, 2006; In Final Form: August 9, 2006

We present a theoretical study of CO_{ad} electrooxidation on Pt nanoparticles. Effects of size and surface texture of nanoparticles on the interplay of relevant kinetic processes are investigated. Thereby, strong impacts of particle size on electrocatalytic activities, observed in experiments, are rationalized. Our theoretical approach employs the active site concept to account for the heterogeneous surface of nanoparticles. It, moreover, incorporates finite rates of surface mobility of adsorbed CO. As demonstrated, the model generalizes established mean field or nucleation and growth models. We find very good agreement of our model with chronoamperometric current transients at various particle sizes and electrode potentials (Maillard, F.; Savinova, E. R.; Stimming, U. *J. Electroanal. Chem.*, in press, doi:10.1016/j.jelechem.2006.02.024). The full interplay of on-site reactivity at active sites and low surface mobility of CO_{ad} unfolds on the smallest nanoparticles (~2 nm). In this case, the solution of the model requires kinetic Monte Carlo simulations specifically developed for this problem. For larger nanoparticles (>4 nm) the surface mobility of CO_{ad} is high compared to the reaction rate constants, and the kinetic equations can be solved in the limiting case of infinite surface mobility. The analysis provides an insight into the prevailing reaction mechanisms and allows for the estimation of relevant kinetic parameters.

1. Introduction

Reduction of cost and optimization of efficiency and of power density are major hurdles toward the commercialization of polymer electrolyte fuel cells (PEFCs). The electrocatalyst, in particular on the cathode side, is the most delicate component in this context. Since the introduction of PEFCs by Grubb in the 1960s,¹ Pt or Pt alloys have been the catalyst of choice due to their high activity and stability. Despite tremendous efforts in research, cheaper catalyst materials exhibiting roughly similar activities to Pt have not been found.

During the last 10–20 years, significant progress has been achieved through the use of highly dispersed Pt nanoparticles with size distributions in the range of 1–10 nm, supported on a micro-to-mesoporous carbon substrate. The small particle sizes provide a vastly enhanced surface area per unit mass of Pt in comparison to previously used Pt blacks.¹ Moreover, impregnation of the porous catalyst layers with a proton-conducting ionomer facilitates the proton transport in them while a sufficient amount of gas pores should still be available for supplying gaseous reactants. These attributes enable larger penetration depths of the reaction zone and better overall utilization of the catalyst at the macroscopic scale. Together these morphological

modifications resulted in a 10–20-fold reduction in Pt content.² As a result, current catalyst layers are, however, complex three-phase composites. Reaction rates in them are distributed in a complex nonuniform fashion at the mesoscopic and microscopic scales.

Naturally, the question arises whether further warranted enhancements of activity per unit mass of catalyst could be achieved with conventional catalyst layer design. Due to statistical constraints, the upper limit of catalyst utilization in completely random three-phase composite structures lies at around 20%. In those structures, at least 80% of the catalyst is not utilized.³

Further detrimental factors for catalyst utilization arise at subordinate structural levels, i.e., in water-filled agglomerates of Pt/C⁴ and at the nanoparticles themselves. Focusing on the latter effects, the average activity per surface site on the catalyst can be estimated, but very little is known about the actual activity of different types of surface sites on nanoparticles. Very likely, the overall activity stems from only a fraction of highly active sites whereas the remaining surface sites have low activity. Hence, specifically tailored, nanostructured catalyst materials could effectuate further improvement of catalytic activity. Clearly, detailed knowledge of the surface morphology and of the relevant reaction processes is required to achieve this goal.

The strong effect of surface morphology on catalytic activity, which is usually manifested as a particle size effect, was shown for different relevant reactions. The fraction of specific surface

* Author to whom correspondence should be addressed. E-mail: meikerl@sfu.ca.

[†] Simon Fraser University.

[‡] National Research Council Canada.

[§] Laboratoire d'Electrochimie et de Physico-chimie des Matériaux et des Interfaces.

^{||} Boreskov Institute of Catalysis.

TABLE 1: Characteristics of Pt Electrodes Used for the Potential Step Experiments^a

sample	method of preparation	loading ($\mu\text{g cm}^{-2}$)	surface area (cm^{-2})	$\bar{d}_N = \sum_i N_i d_i / \sum_i N_i$ (nm)	$\bar{d}_S = \sum_i N_i d_i^3 / \sum_i N_i d_i^2$ (nm)	σ (%)	ref
Pt/GC#a	WCD	1.8	1.07	1.8	2.3	29	20
Pt/GC#b	WCD	5.4	1.81	3.3	5.3	47	20
Pt/GC#c	electrodeposition		0.93	<i>b</i>			19

^a For details, see the original publications. Adapted from refs 19 and 20 with permission from the Royal Society of Chemistry and Elsevier, respectively. ^b Pt electrodeposits comprised of 5–7 nm Pt nanocrystals, which (in contrast to nanoparticles obtained through WCD) were connected to each other via grain boundaries and formed larger 25–100 nm structures.

sites, e.g., edge sites, corner sites, or sites on particular crystalline facets, is a strong function of particle size.^{5,6} As shown by electronic structure calculations, this surface nanostructuring triggers deviations of the electronic structure on the surfaces of small metal clusters from those of well-defined single-crystalline surfaces.^{7,8} The extent and detailed mechanisms of these particle size effects are, however, barely understood. Various reactions relevant to fuel cell operation exhibit diverging trends on activity upon variations of nanoparticle sizes. Experiments have shown that the mass activity of Pt for the oxygen reduction reaction passes through a maximum for a particle size of ~ 3 nm.^{9–11} For methanol oxidation, a decrease in activity for decreasing Pt nanoparticle sizes was found.^{10,12,13} In the case of hydrogen evolution on Pd, however, an increase of the turnover rate by 2 orders of magnitude was observed for particle sizes decreasing from 10 to 1 nm.¹⁴

In the present work, we explore theoretical approaches for CO_{ad} monolayer (ML) oxidation on Pt nanoparticles. Recent studies with model electrocatalysts have revealed strong effects of particle size and morphology on the electrocatalytic activity for CO_{ad} electrooxidation.^{13,15–23} Despite the importance of CO_{ad} electrooxidation as a prototype electrochemical reaction and as a mechanism of poisoning in fuel cell operation, a detailed picture of the reaction processes is still lacking. In the past, most of the understanding of the pertinent reaction mechanism was obtained from single-crystal measurements with defined surface structures under ultra-high-vacuum (UHV) conditions.^{24–29} These studies provided convincing evidence that steps on single-crystal surfaces act as active sites where oxygen is preferentially adsorbed and CO_{ad} oxidation occurs. Experimental results from the Koper group^{30–32} prove that CO_{ad} electrooxidation is also activated at steps. Moreover, Koper and co-workers have shown that CO_{ad} electrooxidation kinetics on stepped Pt single crystals can be reasonably explained in the limit of infinitely fast CO_{ad} surface mobility.³⁰ However, some experimental results, e.g., peak multiplicity in CO_{ad} stripping voltammetry at submonolayer³¹ and saturation coverages,³³ still have not found their explanations, and some authors argue in favor of restricted CO_{ad} surface mobility at solid/liquid electrified interfaces.³⁴

Recent detailed studies demonstrate that the knowledge from the extensively studied, well-defined single-crystal surfaces cannot simply be transferred to the technically relevant nanoparticle structures. From the analysis of CO_{ad} electrooxidation transients, Maillard et al. find severely restricted CO_{ad} surface mobility for nanoparticles smaller than 4 nm.¹⁷

The present study seeks to quantitatively describe the kinetics of CO_{ad} electrooxidation on supported metal nanoparticles and to explore the influence of active sites. In our approach, we separate the surface into domains of active and inactive sites. On the active sites, we consider a detailed mechanism of CO_{ad} electrooxidation via OH_{ad} formation and recombination with CO_{ad}. Further, given the surface structure, the CO_{ad} surface mobility defines the time for the CO_{ad} on inactive sites to reach the active sites. Accordingly, the overall kinetics are the result

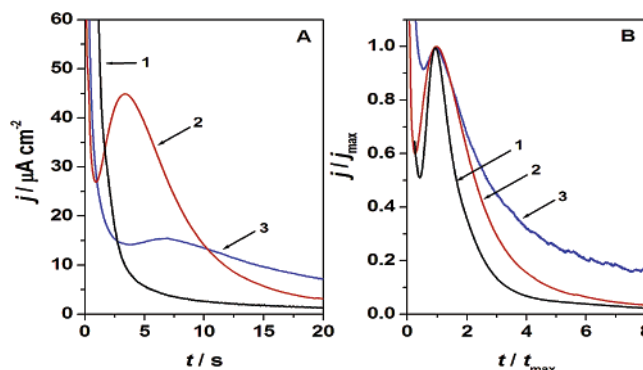


Figure 1. (a) Chronoamperometric transients for different particle sizes at $E = 0.78$ V. Normalized plots are shown in part b. The average particle sizes \bar{d}_N for the graphs shown are (1) > 5 nm, electrodeposited particles, (2) 3.3 nm, and (3) 1.8 nm. The transients are replotted from refs 17 and 20 with permission from the Royal Society of Chemistry and Elsevier, respectively.

of the interplay between on-site reactivity and CO_{ad} surface mobility. The model accounts very well for the experimental transients observed on well-defined model nanoparticle electrodes in refs 17 and 20 and provides a spatial and temporal resolution of the involved processes. In the theoretical assessment, we do not attempt to reveal the fundamental origin of the particle size effects as this has to be left to detailed electronic structure calculations, but our approach rationalizes the contributions of distinct elementary reaction steps and the role of the surface structure. The approach taken is quite general and is easily extended to other reactions. It allows identification of the major causes of nanoparticle effects and provides evaluation criteria for the studied catalyst material in terms of kinetic and structural parameters. The rewards of a successful implementation of specifically tailored, nanostructured catalysts will be significant, as the effects can extend to orders of magnitudes and not mere percentages of improvement.^{14,17}

2. Chronoamperometric Transients for CO Monolayer Oxidation on Pt Nanoparticles

Chronoamperometric transients for CO monolayer oxidation on Pt nanoparticles supported on glassy carbon (GC) have been described in refs 16, 17, and 20. To identify the impact of the particle size and structure, different preparation strategies have been employed in these studies. Nanoparticles with the sizes of 1.8 and 3.3 nm were produced by wet chemical deposition (WCD), while larger particles were produced by electrodeposition. The details of the preparation procedures as well as some representative transmission electron microscopy images can be found in the original publications.^{19,20} A brief description of the samples is given in Table 1.

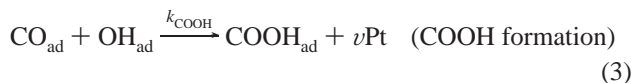
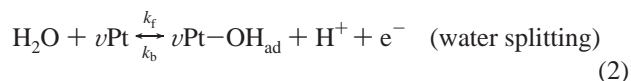
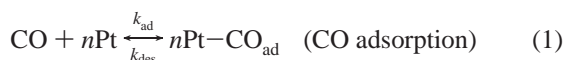
Current transients for CO monolayer oxidation on Pt nanoparticles show the following general features (Figure 1a). Upon stepping the electrode potential into the potential interval above the onset of CO_{ad} oxidation, the current undergoes a fast rise

and decay. Subsequently, a pronounced current maximum develops. The initial current rise and decay is always observed for supported metal nanoparticles but only in some works for extended metal surfaces (e.g., it was reported by Petukhov et al.³⁶ and Korzeniewski et al.³⁷ for Pt(111) but was not found by Lebedeva et al.^{30,31} and Love et al.³⁸ for flat and stepped Pt single crystals and polycrystalline Pt by McCallum et al.³⁹). On carbon-supported metal nanoparticles, it is speculated that this initial current rise represents a superposition of various contributions, including double-layer charging, formation of oxygenated surface groups on carbon, CO oxidation (as confirmed by differential electrochemical mass spectrometry⁴⁰), and anion adsorption.⁴¹ To date, the extent of the different contributions to this initial current decay has not been clarified. The model presented here cannot account for it.

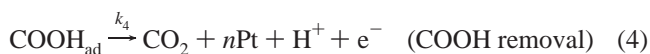
Instead, our analysis focuses on the main current peak, characteristic of a Langmuir–Hinshelwood mechanism, in agreement with previous experiments on well-defined single-crystalline surfaces,^{30–32,36,38,42,43} polycrystalline Pt,^{39,44} or Pt nanoparticles.^{13,15–17,20,22,40} As shown in Figure 1a, the current maximum j_{\max} decreases with decreasing particle sizes, and its occurrence t_{\max} is shifted to longer times. A significant size effect was also found for the current relaxation at long times, as is obvious from Figure 1b. Whereas for the large particles the current peak is only slightly asymmetric and exhibits a fast relaxation, the transients for small particles become highly asymmetric with a pronounced current tailing. For particles of intermediate size, the shape of the transients is a function of the step potential, whereas for the large and small nanoparticles the shape of the transients is not affected by the oxidation potential. The transients become more asymmetric with an increase in the step potential. See ref 20 for further details. In summary, the experimental data shown in Figure 1 indicate that the kinetics of CO_{ad} monolayer oxidation slow down with decreasing particle sizes.

3. Kinetic Model of CO_{ad} Monolayer Oxidation

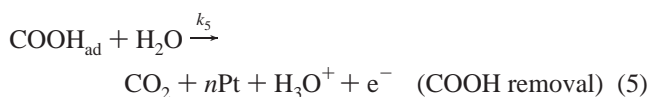
3.1. Reaction Scheme. It is widely accepted that CO_{ad} electrooxidation occurs via a Langmuir–Hinshelwood mechanism and comprises the following general reaction scheme



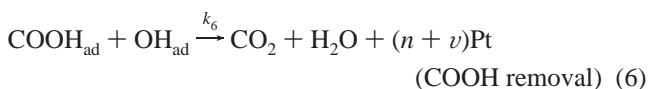
The feasibility of this scheme has been validated by recent density functional theory (DFT) calculations.^{45–48} The electrochemical step of COOH_{ad} removal is, however, still disputed. It may either proceed through a monomolecular electrochemical decomposition step as proposed by Gilman⁴⁹



or through a bimolecular electrochemical reaction as argued by Saravanan et al.⁴⁷

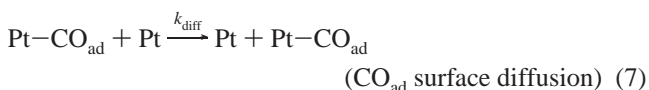


or by a purely chemical step involving an additional OH_{ad}



as suggested by DFT calculations by Anderson et al.^{45,46} The high adsorption energy of CO on Pt leads to high surface coverages of CO_{ad} at adsorption potentials below the onset of water splitting.⁵⁰ It is believed that COOH_{ad} formation, eq 3, involves OH_{ad} and CO_{ad} at adjacent sites. Activation barriers in the range of 0.44–0.58 eV were calculated for this process.^{45,48} The activation barrier for the reverse reaction is 1.18 eV according to ref 48. A Fourier transform IR study by Zhu et al.⁵¹ revealed low concentrations of COOH_{ad} on CO_{ad}-covered Pt surfaces for potentials below ~0.65 V vs reversible hydrogen electrode (RHE). In view of the still debated overall recombination mechanism, we will subsequently consider an effective recombination rate k_{ox} for the sequence of eq 3 and one of the steps in eqs 4–6.

The apparent kinetics of the overall reaction is the result of the interplay of the individual reaction rates for OH_{ad} formation, k_{f} , OH_{ad} back-reaction, k_{b} , eq 2, recombination, k_{ox} , and surface mobility of CO_{ad}, represented by an effective CO_{ad} hopping rate k_{diff} (since we consider OH_{ad} to be immobile, see section 3.2)



The importance of anion coadsorption in CO electrooxidation on Pt(111) and stepped Rh[$n(111) \times (111)$] was examined in ref 52. In the present work, anion adsorption is not considered explicitly, since its effects on reactivity at highly corrugated nanoparticle surfaces are not well understood. We are, however, aware that it may influence the values of the kinetic parameters,²² in particular the rate of surface diffusion, which we obtain from the analysis of experimental data.

3.2. Role of the Surface Structure and Surface Mobilities. Expedient models of CO_{ad} monolayer oxidation on nanoparticle electrocatalysts have to incorporate the heterogeneous surface texture. On ideal particles, e.g., of cubooctahedral shape,^{5,33,53,54} fractions of surface sites at edges, at corners, or on facets are well-defined functions of the particle size. However, it has been speculated recently that metal nanoparticles do not adopt ideal cubooctahedral shapes and defect sites strongly influence the reaction kinetics on their surfaces.²² The particular role of surface defects is, however, poorly understood. Overall, it is likely that the relative fractions of specific geometric sites and defect sites control the net activity generated at the particle surface.

In fact, in experiments on stepped surfaces, CO was found to first adsorb on steps; terrace sites populate only after step sites have been filled. This is valid both for solid/gas^{26,28,29} and solid/liquid electrified interfaces.^{18,55} In UHV, temperature-programmed desorption⁵⁶ and time-resolved IR⁵⁷ measurements on stepped Pt surfaces suggested differences in CO desorption energies of ~0.35 eV for different sites. Theoretical studies support these findings. DFT calculations by Hammer et al. corroborated that CO adsorption energies on stepped Pt(111) are up to 0.7 eV larger at steps than those at terrace sites.^{7,8}

Atomic oxygen also preferentially adsorbs on step and kink sites at solid/gas interfaces.⁵⁸ The same has been proposed for OH_{ad} at solid/liquid electrified interfaces.^{8,32} Consequently, the reaction between CO_{ad} and the oxygenated species on stepped single-crystal surfaces is proposed to preferentially occur at the

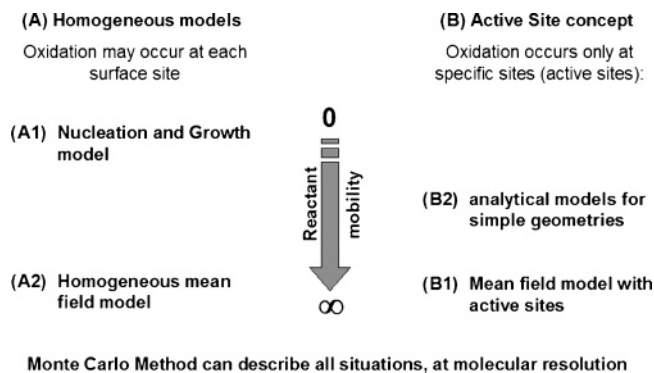


Figure 2. Schemes of different modeling approaches for CO_{ad} monolayer oxidation on Pt catalysts.

step sites.^{29,32,59} On heterogeneous surfaces, the observed particle size effects indicate that the situation may markedly differ from well-defined crystalline surfaces. As a matter of fact, it is still not clear which sites constitute preferential sites for OH_{ad} formation on nanoparticle surfaces. We will subsequently refer to these sites as active sites.

For the reaction between OH_{ad} and CO_{ad} to propagate along the surface, either of them must possess a high surface mobility. Since ab initio calculations indicate that the difference in OH_{ad} adsorption energies for the various adsorption sites exceeds that of CO_{ad},⁴⁶ the former is considered immobile relative to CO_{ad}. Diffusion coefficients for CO_{ad} on Pt single crystals at solid/gas interfaces can be measured by a variety of methods.⁶⁰ The experimentally determined values vary markedly probably due to the influence of the surface heterogeneity and adsorbate coverage. The activation energies for surface diffusion on CO_{ad}/Pt(111) of ~0.3 eV (equivalent to $D_{CO} \approx 10^{-9} \text{ cm}^2 \text{ s}^{-1}$) were determined by He scattering⁶¹ and time-resolved IR spectroscopy.²⁵ In the electrochemical environment, a lower limit of $D_{CO} > 10^{-11} \text{ cm}^2 \text{ s}^{-1}$ on stepped Pt(111) has been postulated by Lebedeva et al. on the basis of kinetic modeling.^{30,32} Relatively high CO_{ad} surface mobilities on atomically flat surfaces may be attributed to minor variations of the adsorption energy for different adsorption sites on extended crystal surfaces (on-top, 2-fold, and 3-fold hollow binding sites) as indicated by ab initio calculations.⁶²

Highly corrugated potential energy landscapes on nanoparticles could strongly affect the surface mobility of CO_{ad}. Indeed, NMR experiments at the solid/gas interface indicate increasing activation energies for surface diffusion with decreasing particle sizes, from 0.27 eV for 10 nm particles to 0.44 eV for 1.2 nm particles.⁶³ Using NMR spectroscopy, Kobayashi et al. have recently provided direct measurement of the tracer diffusion coefficient of adsorbed CO_{ad} on the catalyst surface, D_{CO} , at the solid/electrolyte interface.⁶⁴ The D_{CO} value obtained for Pt black particles (5.5 nm) was equal to $3.6 \times 10^{-13} \text{ cm}^2 \text{ s}^{-1}$, which is considerably smaller than the value previously invoked for single-crystalline surfaces. The reasons for the lower diffusion coefficient at the solid/electrolyte compared to that at the solid/gas interface may be manifold and include (i) anion effects,⁵² (ii) influence of the solvent, or (iii) influence of the surface charge distribution.

3.3. Models of Electrocatalytic Surface Processes. Models of CO_{ad} monolayer oxidation fall into two major categories, homogeneous and heterogeneous surface models, as explained in Figure 2. Homogeneous surface models usually result in simple analytical solutions for the current transients. Assuming equivalence of all surface sites and infinite mobility of

adsorbates leads to the mean field (MF) approximation, model A2 in Figure 2. This model has found widespread use in describing CO_{ad} electrooxidation on low-index^{31,43,65} and high-index single-crystalline surfaces.^{30,32,59}

At the other limit of the mobility scale, the assumption of immobile adsorbates on a homogeneous surface results in the so-called nucleation and growth (N&G) models, model A1 in Figure 2.^{39,66} Early kinetic studies on CO_{ad} electrooxidation have adopted the N&G approach,^{38,39} for both monocrystalline³⁸ and polycrystalline surfaces.³⁹ Within this approach, a transition from progressive (bell-shaped peak) to instantaneous (asymmetric peak) nucleation is predicted upon an increasing step potential, which could explain the experimental observations. In these studies, the N&G model reproduces the general shape and the occurrence of the main current peak quite well. However, according to Koper and co-workers,^{30,59} the N&G model provides inferior quality when fitting the experimental data on CO_{ad} ML oxidation on stepped Pt single crystals. Furthermore, it contradicts experimental evidence that CO_{ad} surface mobility is fast on extended Pt surfaces; see section 3.2.

More general approaches toward CO_{ad} oxidation on homogeneous surfaces consider the influence of CO_{ad} surface diffusion on the overall kinetics.^{36,59,67–69} In general, the balance equations for the kinetics were solved using kinetic Monte Carlo (kMC) simulations. Assuming that CO_{ad} surface diffusivity is potential-independent, Petukhov's studies predict a transition with increasing step potential from symmetric current transients in the MF limit ($k_{\text{diff}}/k_{\text{ox}} \rightarrow \infty$) to asymmetric current transients in the limit of instantaneous N&G ($k_{\text{diff}}/k_{\text{ox}} \rightarrow 0$), consistent with experimental findings.^{36,67} This model assumes fast OH formation and therefore does not account for free surface sites. Upon CO_{ad} + OH_{ad} recombination, OH_{ad} instantaneously replenishes the generated free sites, and diffusion occurs by exchange of OH_{ad} and CO_{ad} on neighboring sites. Koper et al.⁶⁸ explored the implications of a finite CO_{ad} surface diffusion rate on potential step and cyclic voltammetry (CV) simulations. They conjecture that the sharp oxidation peak found in the cyclic voltammograms may reflect fast CO_{ad} diffusion. They argued that the change in the slope of t_{max} versus E found experimentally³⁸ could be attributed to the influence of the OH_{ad} back-reaction at low step potentials. Zhdanov et al.⁶⁹ consider CO_{ad} interaction in their study of CO_{ad} electrooxidation. Their calculations indicate that CO_{ad} interaction can lead to the formation of CO_{ad} islands and a decrease in the overall reactivity.

Heterogeneous surface models (right side in Figure 2) are more generally applicable since they incorporate effects of heterogeneous surface structure and limited surface mobility of adsorbates. In the pertinent literature, these models have not found widespread use for explaining electrocatalytic processes. Although Lebedeva et al.³⁰ identify step sites as the only oxidation sites from their experiments on stepped Pt surfaces, they essentially use a homogeneous MF model to analyze their data. In a subsequent publication from this group,⁵⁹ the effect of finite CO_{ad} hopping rates between step and terrace sites is discussed. It is argued that in potential step simulations these finite hopping rates can result in an increased current tailing. Korzeniewski et al.³⁷ discuss possible influences of active sites.

Maillard et al.¹⁷ have recently presented an analytical study including surface structure effects on nanoparticles. The present model builds on the findings of this approach and represents its generalization.

Bimetallic catalyst surfaces represent systems with inherent surface heterogeneity. To describe CO electrooxidation on PtRu

bimetallic catalysts, the well-known bifunctional mechanism is usually invoked.⁷⁰ It implies that Ru sites on the surface act as nucleation centers for the formation of OH_{ad} that facilitates the oxidation of CO_{ad} from neighboring Pt sites. A lattice gas model for the CO_{ad} electrooxidation from a PtRu surface based on this mechanism has been explored by Koper et al. in ref 71. The approaches considered here are similar to those in ref 71 if one identifies active sites on monometallic Pt particles with Ru atoms on the surface of PtRu catalysts. The Monte Carlo program and the MF approach presented below have, however, been specifically developed for the confined geometry of the nanoparticle surface. Particle size is the main parameter in terms of which we will analyze the interplay between surface diffusion and on-site kinetics.

3.4. Active Site Concept. Clearly, models of electrocatalytic activity at nanoparticles should account for distributions of relevant rates between different sites on the heterogeneous particle surface. A simplified approach is to use a two-state model with fractions ξ_{tot} of electrocatalytically active sites and $(1 - \xi_{\text{tot}})$ of inactive sites on the catalyst surface. Active sites are exclusive sites at which OH_{ad} can be formed, whereas water splitting at inactive sites is deemed unlikely under feasible experimental conditions. (Obviously, at high enough anodic potentials, oxygen species can cover the whole electrode surface. Here, however, we discuss the reaction at lower oxidation potentials, at and slightly above the onset of CO_{ad} ML oxidation.)

This strongly simplified active site concept incorporates the formation of preferential reaction centers on heterogeneous catalyst surfaces with a minimal number of parameters. With only a fraction of the total surface constituting reaction centers, surface diffusion of reactants to these sites becomes a pivotal process, leading to a complex interplay of reactant surface mobility and on-site reactivity.

A full analytical treatment of such an active site model for CO_{ad} electrooxidation can be obtained only with a number of simplifying assumptions. Such a solution was presented in ref 17. This model includes limited diffusivity of CO_{ad} on a circular domain toward active sites on the domain's circumference. A comparison with potential step measurements showed that the model reproduces major experimental trends. The model also has major restrictions: The continuum approach to surface diffusion and the simple surface geometry cannot reproduce more realistic distributions of active sites. Moreover, the active site fraction ξ_{tot} and the recombination rate k_{ox} cannot be determined independently, since in the model only their product is significant. Nevertheless, it gives a useful guideline for preliminary parameter evaluation and has shown good consistency with experimental data. In particular, it corroborated the idea of low CO_{ad} surface mobility on small catalyst particles.

Detailed studies of surface processes, which incorporate heterogeneous surface geometries and finite surface mobilities of reactants, require kMC simulations. This stochastic method has been successfully applied in the field of heterogeneous catalysis on nanosized catalyst particles.^{69,72} Since these simulations permit atomistic resolution, any level of structural detail may easily be incorporated. Moreover, with the kMC technique, simulations proceed in real time. The simulation of current transients or cyclic voltammograms is, thus, straightforward.⁶⁸

Although exploring the effects of finite surface mobility is a focal point of this work, we will consider first a MF approximation with active sites in the limit of fast CO_{ad} surface

diffusion. This simplification allows for a straightforward deterministic formulation of the kinetic equations with obvious meanings of the relevant parameters. It serves as an important reference case for the Monte Carlo procedure. Assuming infinite surface mobility of adsorbates, their individual positions are irrelevant, and the kinetics will be described in terms of surface coverages of the adsorbates. Systematic fitting procedures can be used with this model, which can provide starting values for more elaborate fitting of experimental data with the Monte Carlo approach.

With experiments indicating high CO_{ad} mobility on extended, planar surfaces, this MF approximation provides an adequate approach for the description of the CO_{ad} electrooxidation kinetics on stepped single-crystal surfaces. Moreover, in the limit of large particle sizes, we may assume that the electronic properties of the surface atoms approach those of extended, planar Pt interfaces. Therefore, the MF approach lends itself to the analysis of large nanoparticles. In section 4.1, where the models are compared to experimental data, we will quantify the range of particle diameters and electrode potentials for which the large particle limit is applicable.

3.4.1. Mean Field Model with Active Sites. In this approach, CO_{ad} surface mobility on inactive sites is assumed to be infinitely fast while OH_{ad} on active sites is considered immobile (model B1 in Figure 2). The state variables of the model are the surface coverages of CO_{ad}, θ_{CO} , on inactive sites and the fractions of CO_{ad}-free active sites, θ_{ξ} , and of active sites covered by OH_{ad}, θ_{OH} . In general, these coverages are functions of time and location on the catalyst surface. They represent local average coverages. The ranges of variation are $0 \leq \theta_{\text{CO}} \leq 1$, normalized to the saturation coverage on inactive sites, as well as $0 \leq \theta_{\text{OH}} \leq 1$ and $0 \leq \theta_{\xi} \leq 1$, both normalized to the saturation coverage on active sites. Note that the saturation CO_{ad} coverage is a function of the surface structure.^{33,50}

On nanoparticles, the exact fraction of active sites and the kinetics of their formation are unknown. In view of this unclear situation, a simple and physically sound assumption is to introduce an additional rate constant that describes the removal of CO_{ad} from active sites by nucleation, i.e., without reacting with a neighboring OH_{ad}. We thus define a process for the initial formation of free active sites by removal from CO_{ad} on active sites. This nucleation process is assumed to follow the first-order nucleation law

$$\nu_{\text{N}} = k_{\text{N}}(1 - \theta_{\xi}) \quad (8)$$

Here, k_{N} is the rate constant of nucleation. The nucleation process largely determines the onset of the main current peak and therefore the value of t_{max} .

As the physical equivalent of eq 8 is not readily available, its introduction requires further explanation. In their DFT study on the initiation of CO_{ad} electrooxidation of a CO_{ad} monolayer on a cluster surface, Dunietz et al.⁷³ found that an Eley–Rideal mechanism, for which a water molecule in the electrolyte oxidizes CO_{ad} from a full layer, is rather unlikely. They suggested that a vacant site, e.g. a defect site, must be present to commence the monolayer oxidation. Experimental transients may be fitted with $\theta_{\xi}^0 > 0$ and $k_{\text{N}} = 0$, but the resulting θ_{ξ}^0 will be in the range of 10^{-4} – 10^{-5} at low step potentials. These are unreasonably low values, given that for small nanoparticles the total number of surface atoms is on the order of 10^2 . Due to the lack of more detailed knowledge of the processes at active sites, with eq 8 we have chosen a simple variant for the initial removal of CO_{ad} on active sites. It complies with a scenario suggested by Yates from experiments on stepped surfaces, where

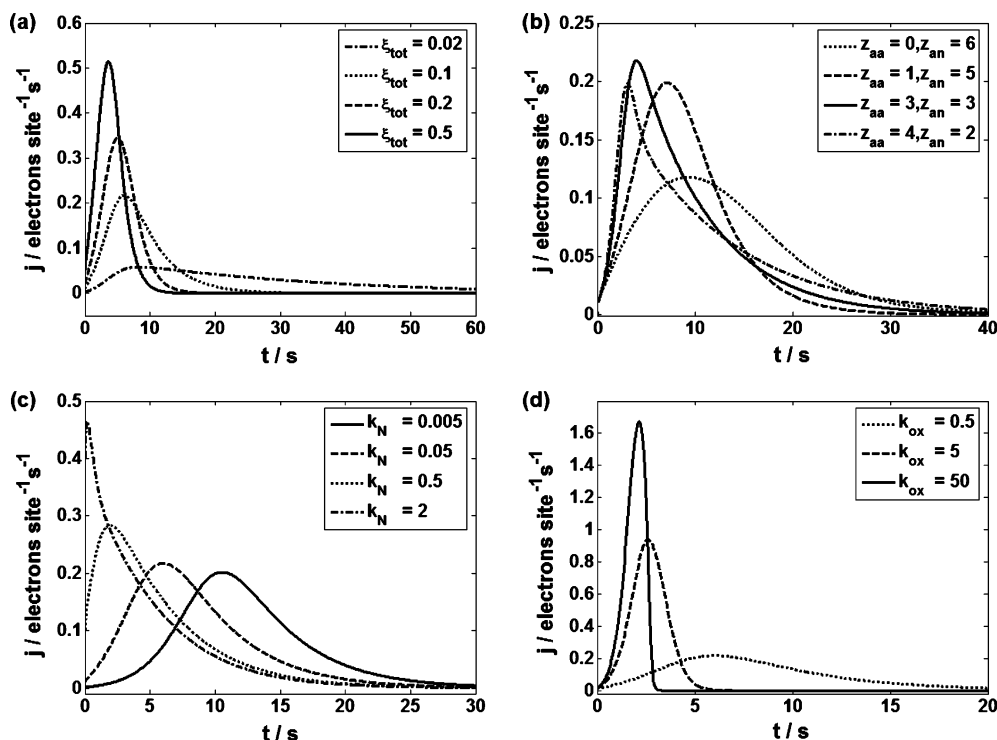


Figure 3. Simulated current transients according to the MF model with active sites. The values of the parameters if not mentioned in the respective legend are $\xi_{\text{tot}} = 0.1$, $k_{\text{ox}} = 0.5 \text{ s}^{-1}$, $k_N = 0.05 \text{ s}^{-1}$, $k_f = 10 \text{ s}^{-1}$, $k_b = 1 \text{ s}^{-1}$, $z_{\text{aa}} = 1.5$, and $z_{\text{an}} = 4.5$, with $\mu^{a \leftrightarrow n} = 0$.

CO_{ad} on the steps is replaced by O_{ad} formed in the steps and moved to terrace sites.²⁹ Thus, eq 8 provides a versatile description of the initial oxidation stage with one single parameter.

On free active sites, we consider the full balance of OH_{ad} coverage, involving OH_{ad} formation with rate ν_f , back-reaction of OH_{ad} to H₂O with rate ν_b , and electrooxidation of CO_{ad} with OH_{ad} with rate ν_{ox} . For the latter, we distinguish between oxidation of CO_{ad} adsorbed on active sites, $\nu_{\text{ox}}^{a \rightarrow a}$, and oxidation of CO_{ad} adsorbed on neighboring inactive sites, $\nu_{\text{ox}}^{a \rightarrow n}$. Finally, CO_{ad} desorption is not considered explicitly since it is slow in comparison to nucleation. According to the literature data, in the absence of dissolved CO, CO_{ad} is irreversibly adsorbed at the solid/electrolyte interface.^{7,54} The corresponding equations are

$$\begin{aligned} \frac{d\theta_{\xi}}{dt} &= \nu_N + \nu_{\text{ox}}^{a \rightarrow a} + \mu^{a \leftrightarrow n} \\ &\quad k_N(1 - \theta_{\xi}) + z_{\text{aa}}k_{\text{ox}}(1 - \theta_{\xi})\theta_{\text{OH}} + \mu^{a \leftrightarrow n} \\ \frac{d\theta_{\text{CO}}}{dt} &= \frac{\xi_{\text{tot}}}{1 - \xi_{\text{tot}}} [-\nu_{\text{ox}}^{a \rightarrow n} + \mu^{a \leftrightarrow n}] = \\ &\quad \frac{\xi_{\text{tot}}}{1 - \xi_{\text{tot}}} [-z_{\text{an}}k_{\text{ox}}\theta_{\text{CO}}\theta_{\text{OH}} + \mu^{a \leftrightarrow n}] \\ \frac{d\theta_{\text{OH}}}{dt} &= \nu_f - \nu_b - \nu_{\text{ox}}^{a \rightarrow n} - \nu_{\text{ox}}^{a \rightarrow a} = \\ &\quad k_f[\theta_{\xi} - \theta_{\text{OH}}] - k_b\theta_{\text{OH}} - z_{\text{an}}k_{\text{ox}}\theta_{\text{CO}}\theta_{\text{OH}} - z_{\text{aa}}k_{\text{ox}}(1 - \theta_{\xi})\theta_{\text{OH}} \end{aligned} \quad (9)$$

All rate constants k_f , k_{ox} , k_N , and k_b are defined per individual process and per second. They are assumed to be potential-dependent. z_{an} and z_{aa} are average numbers of nearest neighbors of an active site with either inactive sites or active sites. Introducing z_{an} and z_{aa} allows for a more detailed representation

of the surface structure in the model. The term $\mu^{a \leftrightarrow n}$ accounts for CO_{ad} diffusion between neighboring active and inactive sites

$$\begin{aligned} \mu^{a \leftrightarrow n} &= \mu^{a \rightarrow n} - \mu^{n \rightarrow a} = \\ &\quad z_{\text{an}}k_d^{a \rightarrow n}(1 - \theta_{\xi})(1 - \theta_{\text{CO}}) - z_{\text{an}}k_d^{n \rightarrow a}\theta_{\text{CO}}(\theta_{\xi} - \theta_{\text{OH}}) \end{aligned} \quad (10)$$

where $k_d^{a \rightarrow n}$ and $k_d^{n \rightarrow a}$ are the rate constants for hopping of CO_{ad} from active to inactive sites and vice versa. The free active site portion available for OH_{ad} formation is $(\theta_{\xi} - \theta_{\text{OH}})$. The measured current upon a potential step is

$$j = e_0\gamma_s\xi_{\text{tot}}(\nu_{\text{ox}}^{a \rightarrow a} + \nu_{\text{ox}}^{a \rightarrow n} + 2\nu_N + \nu_f - \nu_b) \quad (11)$$

where $e_0 = 1.602 \times 10^{-19} \text{ C}$ is the elementary charge and γ_s is the atomic density of the catalyst surface ($\gamma_s \approx 1.5 \times 10^{15} \text{ cm}^{-2}$ for Pt(111)).

It is assumed that each nucleation step involves the transfer of two electrons, one for the OH_{ad} formation and the other for the net process of the COOH_{ad} formation and removal steps; cf. eqs 2–3. In general, the system of differential equations (eq 9) must be solved numerically. Nevertheless, analytical solutions can be found under certain simplifying assumptions.

The basic shape of the transients is largely determined by the surface structure, i.e., the parameters ξ_{tot} , z_{aa} , and z_{an} . This becomes apparent from the simulations obtained with eqs 9–11 for a base parameter set specified in the caption of Figure 3. The value of ξ_{tot} has a strong influence on the symmetry of transients (Figure 3a). Highly symmetric transients with large j_{max} are obtained for large active site fractions. Strong tailing along with a small j_{max} is observed for low values of ξ_{tot} . The effect of varying effective numbers of nearest neighbors z_{aa} and z_{an} is depicted in Figure 3b. Increasing z_{aa} results in a narrower peak, shifted to smaller t_{max} , but with an increased

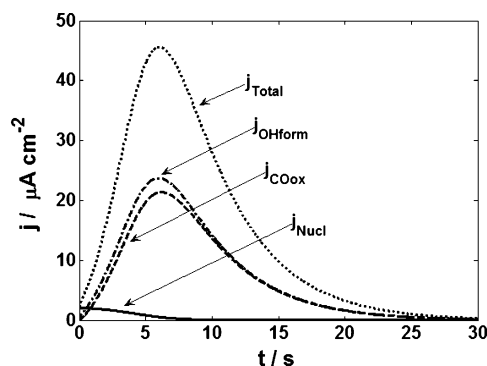


Figure 4. Influence of the individual contributions to the total current transient (dotted curve) in the MF model: nucleation current (solid), current due to the recombination step (dashed), and the OH formation current (dash-dotted). Parameter values are $\xi_{\text{tot}} = 0.1$, $k_{\text{ox}} = 0.5 \text{ s}^{-1}$, $k_{\text{N}} = 0.05 \text{ s}^{-1}$, $k_{\text{f}} = 10 \text{ s}^{-1}$, $k_{\text{b}} = 1 \text{ s}^{-1}$, $z_{\text{aa}} = 1.5$, $z_{\text{an}} = 4.5$, and $\mu^{\text{a} \rightarrow \text{n}} = 0$.

tailing. The steep current increase for high z_{aa} is due to the facilitated oxidation of CO_{ad} on the active site clusters.

An increase in k_{N} shifts the time of the peak maximum to shorter times, until it disappears for $k_{\text{N}} \gg k_{\text{ox}}$, so that the transient only consists of a decaying branch (Figure 3c). At this point, one might speculate whether the observed initial current decay (section 2) might be due to a second type of active site with a very large nucleation rate. This option is not explored here. When k_{ox} is increased, peaks become narrower, and the descending part of the transient becomes steeper as long as recombination and not OH_{ad} formation is rate-determining. The latter case will lead to a steep current falloff past the maximum (Figure 3d). Transients with $k_{\text{ox}} \gg k_{\text{f}}$ have not been observed in experiments. Changes of k_{f} and k_{b} relative to the OH_{ad} equilibrium potential $E_{\text{OH}}^{\text{eq}}$, for which $k_{\text{f}} = k_{\text{b}}$, will affect the peak height and t_{max} . Larger values of k_{ox} or of $k_{\text{f}}/k_{\text{b}}$ result in steeper transients with reduced tailing. The tailing effect is opposite for the nucleation process, where an increase in k_{N} will lead to a more pronounced current tailing. In general, the current tailing resulting from the on-site kinetics alone will be potential-dependent, but its potential variations can be small or even negligible as the effect of k_{N} compensates for the effects of k_{ox} , k_{f} , and k_{b} .⁷¹

In Figure 4, the individual current contributions of the nucleation, OH_{ad} formation, and the recombination processes are shown. Although nucleation is a key process for overall kinetics as it triggers all the other processes, the corresponding current contribution is small. OH_{ad} formation and the recombination currents dominate the overall current generation while the magnitude of the nucleation rate mainly determines the position of the current maximum.

3.4.2. Kinetic Monte Carlo Simulations. The kMC method provides a general technique for the study of surface reactions. Instead of solving a coupled system of deterministic reaction–diffusion equations, the kMC approach is based on a stochastic formulation.⁷⁵ This approach becomes compulsory in order to incorporate details of the heterogeneous catalyst surface structure and effects of finite surface mobilities of CO_{ad} . Every single event in the spatio-temporal evolution (e.g., a reaction or a surface diffusion step) occurs with a defined probability. Hence, the evolution of the system takes the form of a Markovian random walk through configuration space. This method reflects the probabilistic nature of the electrochemical system as a many-particle system. In the present study, we have used a variable step size method as described in ref 76. In the simulations, we consider the same processes as for the MF approach with the

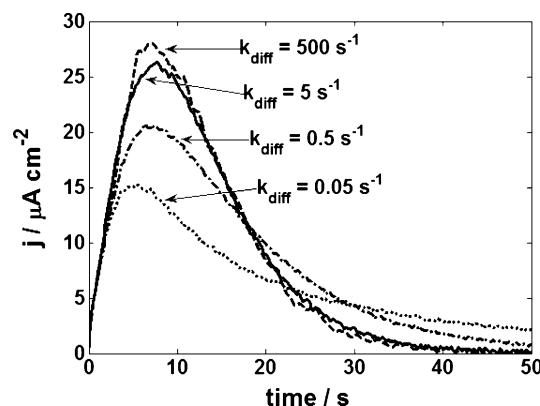


Figure 5. Influence of CO_{ad} surface mobility on the current transient. Parameter values are $\xi_{\text{tot}} = 0.1$, $k_{\text{ox}} = 0.5 \text{ s}^{-1}$, $k_{\text{N}} = 0.05 \text{ s}^{-1}$, $k_{\text{f}} = 10 \text{ s}^{-1}$, $k_{\text{b}} = 1 \text{ s}^{-1}$, $z_{\text{aa}} = 1.5$, and $\mu^{\text{a} \rightarrow \text{n}} = 0$.

addition of CO_{ad} surface diffusion, i.e., the reactions described in eqs 2–7 with rate constants k_{N}^{MC} , k_{f}^{MC} , k_{b}^{MC} , $k_{\text{ox}}^{\text{MC}}$, and k_{diff} . Since the rate constants in eq 9 were defined per site and per second, we have the relations $k_{\text{N}}^{\text{MC}} = k_{\text{N}}$, $k_{\text{f}}^{\text{MC}} = k_{\text{f}}$, and $k_{\text{b}}^{\text{MC}} = k_{\text{b}}$. For the rate constant of recombination, we find $k_{\text{ox}}^{\text{MC}} = k_{\text{ox}}/2$, since a single recombination step of OH_{ad} and CO_{ad} is accounted for by two transition possibilities in the MC procedure, one arising from sampling the OH_{ad} site and the other from sampling the CO_{ad} site. CO_{ad} surface diffusion on active or inactive sites is defined by k_{diff} . Hopping rates between active and inactive sites, $k_{\text{d}}^{\text{n} \rightarrow \text{a}}$ and $k_{\text{d}}^{\text{a} \rightarrow \text{n}}$, can be defined separately.

Let us note further underlying assumptions of this approach. First, the sites are arranged in a hexagonal grid, representing the most abundant nearest neighbor configuration on cubooctahedral Pt nanoparticles.^{5,33,53} The fraction of active sites, ξ_{tot} , is predefined. Active sites could be distributed randomly or deliberately, determining z_{an} and z_{aa} . A simple adlayer structure is considered, in which each site on the model particle is associated with exactly one adsorbate, either CO_{ad} or OH_{ad} .

The influence of CO_{ad} mobility on the current transients is shown in Figure 5. When k_{diff} is decreased, the transients develop a significant tailing along with a decrease of the current maximum.

The kMC approach does not impose any restriction on the CO_{ad} mobility and allows for a detailed representation of the surface structure. It is instructive to compare the active site model to previous model approaches for homogeneous surfaces, i.e., $\xi_{\text{tot}} = 1$: In the limit of fast CO_{ad} mobility, $k_{\text{diff}} \rightarrow \infty$, and with $k_{\text{N}} = 0$ (no nucleation) and fast OH_{ad} formation, the active site model reduces to the well-known homogeneous MF expressions.^{43,67,68,74} At the other end of the CO_{ad} mobility scale, in the case of vanishing CO_{ad} mobility on a homogeneous surface, i.e., with $k_{\text{diff}} = 0$, it can be shown^{37,67} that the current transients from the kMC simulations are equivalent to the general N&G law.^{39,66} Accordingly, the active site model presented here constitutes a generalization of previous model approaches toward structured surfaces with local variations in reactivity.

3.5. Comparison between the MF and the kMC Approaches. In the limit of fast CO_{ad} mobility, $k_{\text{diff}} \rightarrow \infty$, the MC procedure should reproduce transients calculated in the MF approximation, with equal rate constants, except for $k_{\text{ox}} = 2k_{\text{ox}}^{\text{MC}}$. In the MF approach, the constraint of defined adsorbate positions on a given surface structure is waived in favor of a simpler description in terms of effective surface coverages. Structural correlations between positions of active sites are neglected in this approach. The kMC simulations, however,

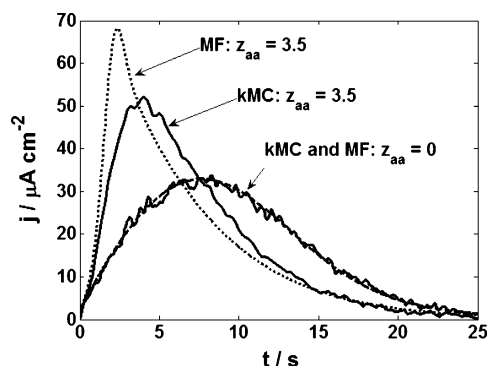


Figure 6. Comparison of kMC simulations with the corresponding MF transient for the case of fast CO_{ad} diffusion with $z_{aa} = 0$ (dashed line) and $z_{aa} = 3.5$ (dotted line). Parameter values are $\xi_{\text{tot}} = 0.1$, $k_{\text{ox}} = 1 \text{ s}^{-1}$, $k_{\text{N}} = 0.05 \text{ s}^{-1}$, $k_{\text{f}} = 10 \text{ s}^{-1}$, $k_{\text{b}} = 1 \text{ s}^{-1}$, $k_{\text{diff}} = 500 \text{ s}^{-1}$, and $\mu^{\text{a} \leftrightarrow \text{n}} = 0$.

explicitly account for such correlations due to the formation of clusters of active sites. The extent of these correlations is determined by z_{aa} and z_{an} as well as by ξ_{tot} . The condition for good agreement between MF and kMC approaches is $z_{aa}k_{\text{ox}} \leq k_{\text{N}}$, for which correlation effects are insignificant. For example, both methods give equivalent transients in the case where $z_{aa} = 0$, as shown in Figure 6. In cases with significant cluster formation of active sites and slow nucleation rates, systematic deviations of the MF results from the kMC simulations are expected (Figure 6). As we will see in section 4, the condition $z_{aa}k_{\text{ox}} \leq k_{\text{N}}$ is hardly fulfilled at low potentials. Nevertheless, the discrepancies between MF and kMC simulations were found to be tolerable.

4. Simulation of Experimental Transients

4.1. Fitted Current Transients for Different Particle Sizes.

In the following, we compare the different modeling approaches with experimental chronoamperometric current transients from refs 17 and 20 and explore their diagnostic capabilities. The electrode potentials are varied in the range of 0.73–0.85 V vs RHE for the small ($\bar{d}_{\text{N}} = 1.8 \text{ nm}$) particles, between 0.68 and 0.85 V for the intermediate ($\bar{d}_{\text{N}} = 3.3 \text{ nm}$) particles, and between 0.63 and 0.8 V for the large ($\bar{d}_{\text{N}} > 5 \text{ nm}$) particles.

The general model, introduced in section 3.4, has 13 independent parameters. Most of them are not well-known. To obtain better significance of the individual parameter values, we tried to eliminate or fix as many parameters as possible in advance. In all calculations we set $k_{\text{d}}^{\text{a} \leftrightarrow \text{n}} = k_{\text{d}}^{\text{n} \leftrightarrow \text{a}} = 0$, i.e., $\mu_{\text{d}}^{\text{a} \leftrightarrow \text{n}} = 0$. Hopping $\text{n} \rightarrow \text{a}$ of CO_{ad} is likely to be slow assuming that CO_{ad} is stronger bound to active sites compared to inactive sites. Hopping $\text{n} \rightarrow \text{a}$ of CO_{ad} seems to be impeded by the preferential chemisorption of OH_{ad} to active sites;²⁹ cf. section 3.2. Moreover, in test calculations with the MF model, it was found that finite but small values of $k_{\text{d}}^{\text{a} \leftrightarrow \text{n}} \leq k_{\text{N}}$ and $k_{\text{d}}^{\text{n} \leftrightarrow \text{a}} \leq k_{\text{N}}$ do not significantly affect the results. The least-squares minimization gives $k_{\text{d}}^{\text{a} \leftrightarrow \text{n}} = k_{\text{d}}^{\text{n} \leftrightarrow \text{a}} = 0$. When $k_{\text{d}}^{\text{n} \leftrightarrow \text{a}}$ and $k_{\text{d}}^{\text{a} \leftrightarrow \text{n}}$ are increased, systematically inferior correspondence between experiment and theory was found. Moreover, the initial coverages were set to $\theta_{\text{S}}^0 = 0$ and $\theta_{\text{CO}}^0 = 1$. Accordingly, the structural parameters ξ_{tot} , z_{an} , and z_{aa} and the kinetic parameters k_{ox} , k_{N} , k_{f} , k_{b} , and k_{diff} were left variable for fitting.

As discussed in section 3.4, the fitting procedure starts with the analysis of the capabilities of the MF model to fit the experimental transients for the electrodes with different mean particle sizes. This allowed us to use straightforward least-

squares routines, in contrast to the intricate curve-fitting procedure with the kMC method. The results for the large, electrodeposited particles in the whole potential range explored were quite satisfactory as shown in Figure 7a. No further improvement of the fits was achieved when k_{diff} was allowed to vary using the full kMC solution. Very good fitting results with the MF model were also obtained for the intermediate particles at $E < 0.8 \text{ V}$ (Figure 7b, the upper two graphs). This approach complies with the experimental evidence of fast CO_{ad} diffusion for extended surfaces; section 3.2. However, for small particles, it was not possible to obtain reasonable quality fits with the MF model in the limit of infinitely fast diffusion. The quality of the fits for the whole data set for small particles, Figure 7c, and for the intermediate particles at $E \geq 0.8 \text{ V}$ (bottom graph in Figure 7b) was substantially improved when the diffusion step was included in the overall reaction scheme and k_{diff} was allowed to vary using the full kMC solution with finite surface mobility. The difference in the MF and the kMC fitting results is exemplified in the middle graph of Figure 7c. Considering the strong influence of the active site fraction on the symmetry of the transients (Figure 3a), we analyzed an alternative scenario in which variations of the active site fraction are considered as the sole origin of differences in the transients for different particle sizes and potentials. The results are not satisfactory. It is not possible to attribute effects of particle sizes and electrode potentials exclusively to changes in the active site fraction. The adequate tailing of transients could not be reproduced. Overall, the active site model provides very good agreement with experimental data. Consistent sets of parameters could be determined for all three particle sizes and at all potentials using the appropriate approach.

Clearly, the active site model shows superior agreement with experimental data compared to alternative model approaches. This is demonstrated in Figure 8, where the fitted current transients obtained from different modeling approaches are compared for a typical experimental transient. A homogeneous MF model as described in refs 30, 59, 67, and 68 cannot reproduce the strong asymmetry in transients and the current tailing at longer times for small particle sizes and high step potentials. The homogeneous MF model inherently gives symmetric transients. Furthermore, our model gives systematically better agreement with experiments than fitting with N&G models.^{38,39,44}

For the large particles, which were formed by a secondary nucleation and contained some amount of nonagglomerated small particles,^{19,20,35} a bump in the tailing of the experimental transients can be observed.²⁰ The difference between measurement and fit (see inset in Figure 7a) results in a current transient that follows similar trends to what could be observed for the intermediate particles. We tentatively attribute this to CO_{ad} monolayer oxidation on nonaggregated nanometer-size Pt. Accordingly, the main peak and the shoulder at longer times are due to the contributions of particle agglomerates and of the nonaggregated particles, respectively. In view of this finding the question arises whether the current tailing for all particle sizes could be explained by effects of the particle size distribution (PSD) alone, assuming unrestricted CO_{ad} mobility. This alternative scenario leads, however, to inconsistent results. On intermediate size particles, it could not explain the transition from transients exhibiting minor tailing to transients with pronounced tailing that occurs at $E \approx 0.8 \text{ V}$. As seen in Figure 7b, the MF approximation with a unimodal PSD reproduces the measurements at $E < 0.8 \text{ V}$ very accurately. Using the same unimodal PSD fails to reproduce the tailing at $E \geq 0.8 \text{ V}$.

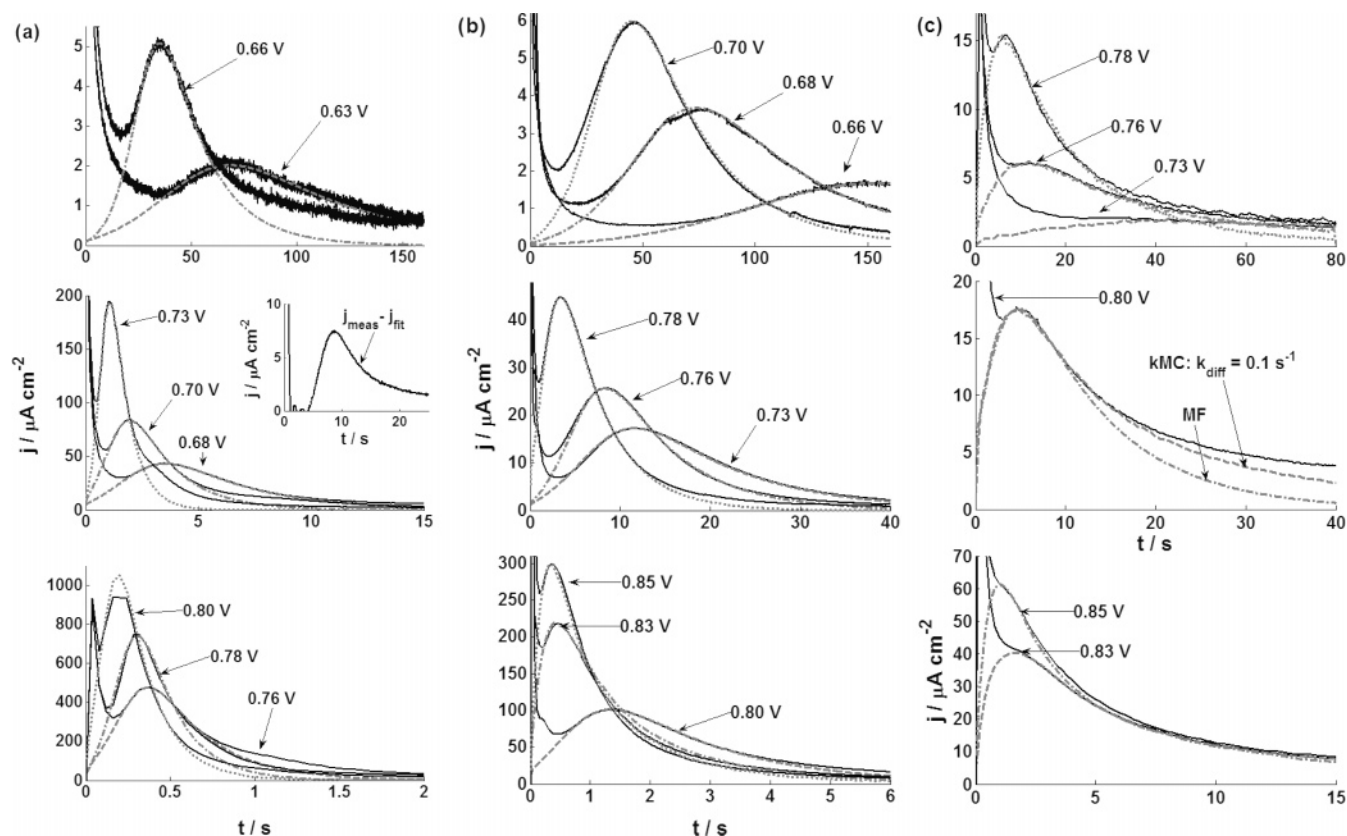


Figure 7. Fits (dotted lines) of the experimental (solid lines) current transients for three particle sizes at different potentials: (a) Large (>5 nm), electrodeposited particles, all fits were obtained using the active site MF model. The inset in the middle graph of part a shows the current transient obtained from the difference between measurement and fit at $E = 0.70$ V. (b) The 3.3 nm (intermediate) particles, the fits in the bottom graph were obtained using kMC simulations. (c) The 1.8 nm (small) particles. For this particle size, kMC simulations were used for fitting. The middle graph in part c shows a comparison of the MF and kMC fits at $E = 0.80$ V. The experimental transients are replotted from refs 17 and 20 with permission from the Royal Society of Chemistry and Elsevier, respectively.

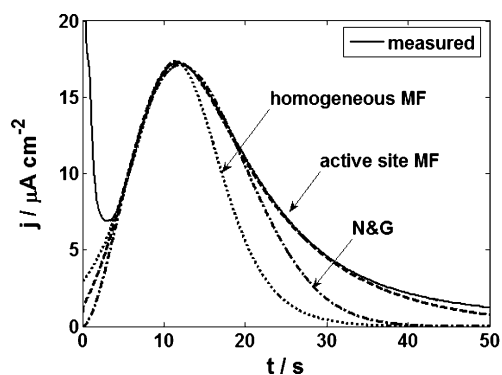


Figure 8. Comparison of the best fits using the homogeneous MF model (dotted line), the N&G model (dash-dotted line) according to refs 39 and 66, and the active site MF model (dashed line) for the current transient at $E = 0.78$ V for the 3.3 nm particles. The experimental transient is replotted from ref 20 with permission from Elsevier.

4.2. Structural Parameters: Nature of Active Sites. Since the exact nature of active sites is not known a priori, ξ_{tot} , z_{an} , and z_{aa} were initially left variable for fitting at the different potentials. For a given particle size, these values did, however, not change significantly over the potential range. Given the small potential variations found for ξ_{tot} , z_{an} , and z_{aa} , they were kept constant in a second run. This allowed further reduction of the number of fitting parameters to k_{ox} , k_{N} , k_{f} , k_{b} , and k_{diff} .

This suggests that active sites are stable in the course of the experiments. Potential-dependent restructuring effects

can be neglected. For the 1.8 and 3.3 nm particles, our calculations suggest $\xi_{\text{tot}} = 0.1$, $z_{\text{aa}} = 1.5$, and $z_{\text{an}} = 4.5$ as reasonable values for the whole potential range. In fact, we have analyzed a further data set (not shown) from ref 17. The fitted values for the structural parameters for this particle size are again in the range of those mentioned above. For the large, electrodeposited particles, $\xi_{\text{tot}} = 0.17$, $z_{\text{aa}} = 2.2$, and $z_{\text{an}} = 3.8$ gave the best agreement over the considered potential range.

It is instructive to compare the value of $\xi_{\text{tot}} \approx 0.1$ found for the small and intermediate particles to the fraction of edge and corner sites on a perfect cubooctahedral crystallite, often alluded to as prospective active sites. For the 1.8 nm particles, the fraction of edge and corner sites accounts for $\sim 50\%$ of the surface sites, whereas the corners alone make up $\sim 12\%$. These fractions diminish for the 3.3 nm particles, to 28% and 2%, respectively.⁵ These values and their variations with particle size are irreconcilable with the fitted values. It seems unlikely that edge and/or corner sites act as active sites. Instead, our findings point toward a scenario where defect sites constitute the active sites. This is in line with the conclusions from the work of the Ross group at Berkeley, who argued that Pt crystallites are not perfect cubooctahedrons^{9,22,33,54} and stressed the importance of defect sites on CO_{ad} electrooxidation kinetics.²²

The higher active site fraction found for the electrodeposited particles reflects the highly corrugated surface morphology due to the nanograin structure of these particles. This results in a relatively high number of defect sites such as sites at grain boundaries of agglomerated particles and steps on their surfaces that may serve as active sites.^{19,35}

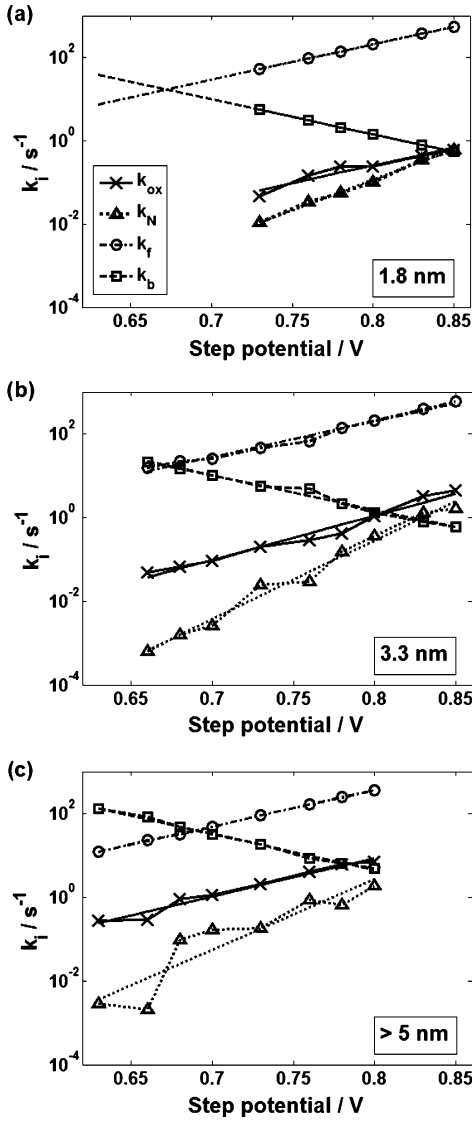


Figure 9. Tafel plots of the electrochemical rate constants k_{ox} , k_{N} , k_{f} , and k_{b} for the three different particle sizes: (a) 1.8 nm (small) particles, (b) 3.3 nm (intermediate) particles, and (c) large electrodeposited (>5 nm) particles. The straight lines in the graphs correspond to fits of the rate constants according to the Tafel law, eq 12.

4.3. Electrochemical Reaction Steps. We seek parametrizations of the electrochemical rate constants k_i with exponential dependence on the electrode potential E (Tafel law)

$$k_i = k_i^0 \exp\left(\frac{\alpha_i F}{RT} E\right) = k_i^0 \exp\left(\frac{E}{b_i}\right) \quad (12)$$

suggested by the simple phenomenological treatment of charge-transfer processes.

Figure 9 displays Tafel plots of k_{ox} , k_{N} , k_{f} , and k_{b} for all three particle sizes. Corresponding parameters are listed in Table 2. The equilibrium potential $E_{\text{OH}}^{\text{eq}}$, electron-transfer coefficients, and preexponential factors (generic rate constants) for the electrocatalytical steps are obtained from the fits in Figure 7. As a general feature from the graphs in Figure 9, the rates are ordered as $k_{\text{f}} \gg k_{\text{ox}} > k_{\text{N}}$. OH_{ad} formation as described by eq 2 represents the fastest process. The relation $(k_{\text{f}}, k_{\text{b}}) \gg k_{\text{ox}} > k_{\text{N}}$ warrants a separation of time scales. Therefore, on the relevant scale of recombination, the OH_{ad} coverage can be considered in a steady state. A full analytical solution can be obtained for this case in the limit of fast CO_{ad} mobility.⁷⁴

TABLE 2: Model Parameters as Extracted from the Fits in Figure 7

particle size	1.8 nm	3.3 nm	> 5 nm
ξ_{tot}	0.1	0.1	0.17
α_{ox}	0.5	0.6	0.5
α_{N}	0.9	1.1	1.0
α_{f}	0.5	0.5	0.5
α_{b}	0.5	0.5	0.5
$E_{\text{OH}}^{\text{eq}}$ (V)	<0.69	0.68	0.68
k_{diff} (s ⁻¹)	0.08–0.15	4	>10
D_{CO} (cm ² s ⁻¹)	10 ⁻¹⁶	5 × 10 ⁻¹⁵	>10 ⁻¹⁴

The water splitting reaction follows a Tafel law with a slope of ~120 mV/decade, i.e., $\alpha_{\text{f}} \approx \alpha_{\text{b}} \approx 0.5$. In consideration of the fact that k_{f} and k_{b} are independent fitting parameters, the result $\alpha_{\text{f}} + \alpha_{\text{b}} \approx 1$ corroborates the validity of our approach. We find $E_{\text{OH}}^{\text{eq}} \approx 0.67$ – 0.69 V for large and intermediate particles, respectively, and we can give an upper limit $E_{\text{OH}}^{\text{eq}} < 0.69$ V for small particles. It is not possible to pin down the exact value of $E_{\text{OH}}^{\text{eq}}$ for this particle size, since only potentials in the range $E \geq 0.73$ V were studied in experiments,²⁰ for which $k_{\text{f}} \gg k_{\text{b}}$. (Due to the overall slow reaction kinetics, the currents measured at lower step potentials were indistinguishable from the background current.) In general, the results for k_{f} and k_{b} show substantial error margins. At electrode potentials $E > (E_{\text{OH}}^{\text{eq}} + 0.05 \text{ V})$, i.e., for $k_{\text{f}} \gg k_{\text{b}}$, the precise values of these parameters are insignificant since OH_{ad} formation is not the rate-limiting process and $\theta_{\text{OH}} \approx 1$. Furthermore, as long as $k_{\text{f}} \gg k_{\text{ox}}$, the absolute values of k_{f}^0 and k_{b}^0 will be afflicted with substantial error margins, as the shape of the transient is largely determined by θ_{OH} .

k_{ox} exhibits a similar or slightly stronger potential dependence compared to OH_{ad} formation with $\alpha_{\text{ox}} \approx 0.5$ – 0.6 . For the given potential range, we find that k_{ox} at a given E decreases with decreasing particle size. They are roughly related by $10(\overline{d_{\text{N}}} > 5 \text{ nm}):2(\overline{d_{\text{N}}} = 3.3 \text{ nm}):1(\overline{d_{\text{N}}} = 1.8 \text{ nm})$. The differences are minor between small and intermediate size particles, but the electrodeposited particles show significantly better recombination kinetics. Hence, the increase of the overall activity with the particle size originates in part from on-site kinetics. However, the major increase of k_{ox} occurs when the structure of nanoparticles changes from single- to multigrain. The latter structures are likely to exhibit a potential energy landscape favorable for the recombination step.¹⁹

The nucleation process shows the strongest potential dependence with $\alpha_{\text{N}} \approx 0.9$ – 1.1 . From this we infer that nucleation does not proceed in a single elementary step. Fitting allows determination of the individual rates of k_{ox} and k_{N} quite accurately. Nevertheless, several factors may obstruct an unequivocal estimate of the rate constants and may thus lead to the scatter of the rates seen in the Tafel analysis (Figure 9), in particular for k_{N} for small particles. The extracted value of k_{N} is essentially determined by the initial stage of CO_{ad} electrooxidation.

4.4. CO_{ad} Surface Mobility. A central result from our findings is that the CO_{ad} diffusion rate decreases with decreasing particle size. Further, in all calculated curves, the potential did only have a minor influence on k_{diff} . We thus consider k_{diff} being potential-independent. In the subsequent discussion, the relation $D_{\text{CO}} \approx k_{\text{diff}} a^2$ is used to convert the hopping rate, k_{diff} , obtained from the kMC simulation, into an effective tracer diffusion coefficient. Here, a is the lattice constant.^{60,77}

We find that on the electrodeposited particles the limiting case with infinite surface mobility provides good results and could not be improved using finite CO_{ad} mobilities. For all

potentials, $k_{\text{diff}} \gg k_{\text{ox}}$. Consequently, fitting can provide only a lower bound $k_{\text{diff}} > 10 \text{ s}^{-1}$, i.e., $D_{\text{CO}} > 10^{-14} \text{ cm}^2 \text{ s}^{-1}$. The overall kinetics on these particles are controlled by the recombination step at all measured potentials.

For the small particles, fitting required a low diffusion rate for CO_{ad} , $k_{\text{diff}} \approx 10^{-1} \text{ s}^{-1}$, resulting in a diffusion coefficient of $D_{\text{CO}} \approx 10^{-16} \text{ cm}^2 \text{ s}^{-1}$, similar to that reported in ref 17. Because $k_{\text{diff}} < k_{\text{ox}}$, the overall kinetics on the small nanoparticles are limited by diffusion of CO_{ad} at all measured potentials.

The intermediate size particles represent the most interesting case as we observe the transition from the case in which overall activity is controlled by on-site kinetics at small electrode potentials toward a control by surface diffusion at step potentials above $E \approx 0.8 \text{ V}$ (i.e., as the recombination rate constant increases and exceeds the diffusion rate constant). From fitting the transients at high potentials with the kMC method, we found $k_{\text{diff}} \approx 4 \text{ s}^{-1}$ or $D_{\text{CO}} \approx 5 \times 10^{-15} \text{ cm}^2 \text{ s}^{-1}$. These results are reflected in the normalized plots of these transients (Figure 6 in ref 20), where a change in the current tailing from a fast decay, typical for large particles, at low potentials to a slow decay, similar to that of small particles, at potentials $E \geq 0.8 \text{ V}$ was observed. Thus, we may identify the slow current decay with a diffusion limitation (potential-independent tailing as k_{diff} is potential-independent), whereas the fast current decay corresponds to the kinetically limited regime.

Overall, the results show that the particle size has a tremendous effect on CO_{ad} mobility. The value of D_{CO} changes by at least 2 orders of magnitude when the particle size is increased from $\bar{d}_{\text{N}} = 1.8 \text{ nm}$ to $\bar{d}_{\text{N}} > 5 \text{ nm}$. Our results are in line with findings from NMR measurements of CO_{ad} mobility on Pt in UHV (see discussion in section 3.2).^{63,64} Thus, differences in apparent reactivity for CO_{ad} electrooxidation at nanoparticles with different sizes but identical preparation methods are predominantly due to the strong size effect on D_{CO} .

At the moment, we can only speculate about the origin of the strongly reduced surface mobility on small particles. The activation energy of surface diffusion is governed by the surface corrugation potential. The latter is determined by the difference in the free energy of adsorption at different surface sites. It has been shown, both experimentally and computationally,⁶² that the strength of CO bonding to Pt sites depends critically on the local surface structure. Clearly, surfaces of small particles are more "heterogeneous", which explains their higher corrugation potential and the effectively reduced surface mobility.

Another relevant aspect is related to the mechanism of surface mobility of CO_{ad} ,⁶⁰ which is always bonded to the surface with its carbon atom. Hopping of CO_{ad} from one on-top position to another occurs via an intermediate bridge-bonded CO_{ad} . Meanwhile, Becerra et al. showed in their NMR work⁶³ that a decrease of the particle size greatly reduces the fraction of bridge-bonded CO_{ad} , thereby inhibiting CO_{ad} mobility. This effect, which was also found by Weaver's group,⁷⁸ may as well be related to the increased surface heterogeneity and the higher curvature of small particles.

5. Conclusions and Outlook

We exploit the active site concept as a simple two-state approach for representing nonuniform reaction rate distributions on heterogeneous nanoparticle surfaces. The model consistently reproduces chronoamperometric current responses of CO_{ad} monolayer oxidation for various particles sizes and electrode potentials.²⁰ In this simple approach, OH_{ad} formation is assumed to be restricted to active sites, while the remaining surface sites

are considered inactive. Thereby, strong particle size effects on catalyst activity for CO_{ad} monolayer electrooxidation can be rationalized.

From the analysis, we found that the active sites are likely to be related to defect sites rather than low-coordination sites of an idealized crystallite structure, because the fraction of active sites remained constant at $\sim 10\%$ for particles in the range of 1.8–3.3 nm and increased only for particles with nanograined structure that have a more corrugated surface.

Splitting of the overall reaction into a nucleation step for CO_{ad} removal from active sites, water splitting, and recombination of OH_{ad} and CO_{ad} enables a refined analysis of the individual processes. All electrochemical steps follow Tafel laws with the water splitting reaction being the fastest reaction. The nucleation step proved to be necessary to model the initial stage of monolayer oxidation. Alternative scenarios based on the introduction of initially free sites could not produce meaningful results. For a given step potential, recombination rates increase with increasing particle size. Hence, part of the overall activity increase for CO_{ad} electrooxidation for larger particles stems from the better on-site kinetics.

Most importantly though, a marked decrease of CO_{ad} mobility with decreasing particle size encompasses the apparent particle size effect. When the particle size is decreased from > 5 to 1.8 nm, the CO_{ad} diffusivity drops by at least two decades, slowing down the oxidation kinetics. These findings are in line with NMR experiments.^{63,64}

The comparison with homogeneous MF and N&G models indicates that they are insufficient for describing the electrochemical kinetics on nanoparticles. As emphasized before, the heterogeneous surface model with active sites and unconstrained surface mobility is in fact a consistent generalization of these two limiting scenarios.

Overall, the model establishes correlations between particle size, heterogeneous surface structures, and kinetic processes. The detailed comparison with a set of experimental data²⁰ provides insight into relevant reaction mechanisms. The surface structure can be characterized, and kinetic parameters of involved processes can be determined. However, to deal with complex many-particle systems and largely random surface structures, this approach has to concede to a number of simplifying assumptions. Indeed, on one hand, surface structure seems to be essential for the electrocatalytic properties of nanoparticles. On the other hand, the surface morphology is difficult to characterize and control in situ. In view of this dilemma, we use this rather abstract model, although the Monte Carlo approach would permit a more detailed representation of the surface structure. The resultant simplifying assumptions might be critically reviewed here: A simple surface model is considered. The three-dimensional particle with its corrugated surface structure is mapped onto a regular hexagonal grid in two dimensions. Reflective boundary conditions account for the confinement of mobile adsorbates on this surface. Variations in activity between distinct sites on the surface are considered by a simple two-state approach, distinguishing between active sites as exclusive sites on which OH_{ad} can form and inactive sites that only serve as a reservoir of strongly adsorbed CO_{ad} , supplied by surface diffusion.

As of today, little is known about the active sites. A refined analysis will critically depend on experiments that are capable of revealing their nature and underlying processes. In this respect, the model would certainly benefit from more detailed electronic structure calculations for systems that could mimic heterogeneous nanoparticle surfaces. Such a calculation could

also form the basis for more refined models in terms of reaction pathways, surface mobility, and rates of the charge-transfer steps.

An important result of this study is the conclusion of the restricted CO_{ad} surface mobility. We hope very much that this work will stimulate further research into CO_{ad} surface diffusion on metal nanoparticles to confirm this conjecture experimentally, e.g., by applying EC NMR. Another important aspect is the lack of understanding of the processes leading to the initial current spike in chronoamperograms. Further studies are necessary for unveiling its origin.

In the present work, the active site model was applied to CO_{ad} monolayer electrooxidation on pure Pt nanoparticles. The employed methods could, however, be readily adapted to other electrocatalytic reactions on heterogeneous catalyst surfaces. A straightforward and insightful extension would be to study CO_{ad} electrooxidation on Pt alloy nanoparticles such as PtRu. This work is in progress. For this system, the active sites can most likely be identified as Ru atoms.⁷¹ Their fraction and distribution on the surface will determine the activity of the catalyst. If the surface composition could be obtained from independent structural characterization, then the analysis of experimental current transients could provide more precise values of kinetic rate constants. Once kinetic parameters are known from reference studies, the method could be used to characterize the surface structure of PtRu alloys of unknown morphology.

For CO_{ad} electrooxidation on Pt or Pt alloys, a wealth of regimes exhibiting instabilities and/or oscillations has been observed.⁷⁹ A stability analysis of the active site model could elucidate the relevant dynamic mechanisms for oscillations and the influence of the surface structure on the stability of CO_{ad} electrooxidation. Surface structure plays a decisive role for stability diagrams of heterogeneous catalytic reactions on nanoparticles.⁸⁰ Comparison of experimental stability diagrams with model results could provide a powerful in situ technique for analyzing morphological changes and degradation phenomena. An important direction to be taken with the present approach is of course to tackle the most critical reactions in PEFCs: oxygen reduction and methanol oxidation.

Acknowledgment. Financial support from a Provincial Research Fellowship of the British Columbia Innovation Council (B.A. and M.E.) and from the France–Canada Research Fund (F.M. and M.E.) is gratefully acknowledged. The authors acknowledge Professor Ulrich Stimming who has hosted three of us (M.E., F.M., and E.S.) for various periods of time in 2001–2004 and who can be considered the “catalyst” of our collaboration.

References and Notes

- (1) Sandstede, G.; Cairns, E. J.; Bagotsky, V. S.; Wiesener, K. In *Handbook of Fuel Cells*; Vielstich, W., Lamm, A., Gasteiger, H., Eds.; John Wiley & Sons: Chichester, U. K., 2003; Vol. 1, pp 145–218.
- (2) (a) Kocha, S. S. In *Handbook of Fuel Cells*; Vielstich, W., Lamm, A., Gasteiger, H., Eds.; John Wiley & Sons: Chichester, U. K., 2003; Vol. 3, pp 538–565. (b) Gottesfeld, S.; Zawodzinski, T. In *Advances in Electrochemical Science and Engineering*; Alkire, R., Gerischer, H., Kolb, D., Tobias, C., Eds.; Wiley VCH: Weinheim, Germany, 1997; Vol. 5, pp 195–301.
- (3) (a) Eikerling, M.; Kornyshev, A. A. *J. Electroanal. Chem.* **1998**, *453*, 89–106. (b) Eikerling, M.; Ioselevich, A. S.; Kornyshev, A. A. *Fuel Cells* **2004**, *4*, 131–140. (c) Eikerling, M.; Kornyshev, A. A.; Kulikovskiy, A. A. *Fuel Cell Rev.* **2004/2005**, (Dec/Jan), 15–25. (d) Eikerling, M.; Kornyshev, A. A.; Kulikovskiy, A. A. In *Encyclopedia of Electrochemistry*; Macdonald, D. D., Ed.; Wiley-VCH: Weinheim, Germany, 2006; Vol. 5, in press.
- (4) Wang, Q.; Eikerling, M.; Song D.; Liu, S. *J. Electroanal. Chem.* **2004**, *573*, 61–69.
- (5) Van Hardefeld, R.; Hartog, F. *Surf. Sci.* **1969**, *15*, 189–230.
- (6) Kinoshita, K. *J. Electrochem. Soc.* **1990**, *137*, 845–848.
- (7) Hammer, B.; Nielsen, O. H.; Nørskov, J. K. *Catal. Lett.* **1997**, *46*, 31–35.
- (8) Hammer, B.; Nørskov, J. K. *Adv. Catal.* **2000**, *45*, 71–130.
- (9) Sattler, M. L.; Ross, P. N. *Ultramicroscopy* **1986**, *20*, 21–28.
- (10) Kabbabi, A.; Gloaguen, F.; Andolfatto F.; Durand, R. *J. Electroanal. Chem.* **1994**, *373*, 251–254.
- (11) (a) Gamez, A.; Richard, D.; Gallezot, P.; Gloaguen, F.; Faure, R.; Durand, R. *Electrochim. Acta* **1996**, *41*, 307–314. (b) Takasu, Y.; Ohashi, N.; Zhang, X.-G.; Murakami, Y.; Minawaga, H.; Sato, S.; Yahikozawa, K. *Electrochim. Acta* **1996**, *41*, 2595–2600. (c) Ross P. N. In *Handbook of Fuel Cells*; Vielstich, W., Lamm, A., Gasteiger, H., Eds.; John Wiley & Sons: Chichester, U. K., 2003; Vol. 2, pp 465–480. (d) Gasteiger, H. A.; Kocha, S. S.; Sompalli, B.; Wagner, F. T. *Appl. Catal., B* **2005**, *56*, 9–35.
- (12) (a) Yahikozawa, K.; Fujii, Y.; Yoshiharu, M.; Katsunori, N.; Takasu, Y. *Electrochim. Acta* **1991**, *36*, 973–978. (b) Frelink, T.; Visscher W.; Van Veen, J. A. R. *J. Electroanal. Chem.* **1995**, *382*, 65–72. (c) Takasu, Y.; Iwazaki, T.; Sugimoto, W.; Murakami, Y. *Electrochem. Commun.* **2000**, *2*, 671–674.
- (13) Cherstiouk, O. V.; Simonov, P. A.; Savinova, E. R. *Electrochim. Acta* **2003**, *48*, 3851–3860.
- (14) (a) Meier, J.; Friedrich, K. A.; Stimming, U. *Faraday Discuss.* **2002**, *121*, 365–372. (b) Eikerling, M.; Meier, J.; Stimming, U. *Z. Phys. Chem.* **2003**, *217*, 395–414.
- (15) Friedrich, K. A.; Henglein, F.; Stimming, U.; Unkauf, W. *Electrochim. Acta* **2000**, *45*, 3283.
- (16) Cherstiouk, O. V.; Simonov, P. A.; Zaikovskii, V. I.; Savinova, E. R. *J. Electroanal. Chem.* **2003**, *554*, 241.
- (17) Maillard, F.; Eikerling, M.; Cherstiouk, O. V.; Schreier, S.; Savinova, E.; Stimming, U. *Faraday Discuss.* **2004**, *125*, 357–377. See also Additions/Corrections at <http://xlink.rsc.org/?DOI=b303911k>.
- (18) Maillard, F.; Savinova, E. R.; Simonov, P. A.; Zaikovskii, V. I.; Stimming, U. *J. Phys. Chem. B* **2004**, *108*, 17893–17904.
- (19) Maillard, F.; Schreier, S.; Hanzlik, M.; Savinova, E. R.; Weinkauff, S.; Stimming, U. *Phys. Chem. Chem. Phys.* **2005**, *7*, 385–393.
- (20) Maillard, F.; Savinova, E. R.; Stimming, U. *J. Electroanal. Chem.*, in press, doi:10.1016/j.jelechem.2006.02.024.
- (21) Mayrhofer, K. J. J.; Arenz, M.; Blizanac, B. B.; Stamenkovic, V. R.; Ross, P. N.; Marković, N. M. *Electrochim. Acta* **2005**, *50*, 5144–5154.
- (22) Arenz, M.; Mayrhofer, K. J. J.; Stamenkovic, V.; Blizanac, B. B.; Tomoyuki, T.; Ross, P. N.; Marković, N. M. *J. Am. Chem. Soc.* **2005**, *127*, 6819–6829.
- (23) Solla-Gullón, J.; Vidal-Iglesias, F. J.; Herrero, E.; Feliu, J. M.; Aldaz, A. *Electrochem. Commun.* **2006**, *8*, 189–194.
- (24) (a) Engel, T.; Ertl, G. *Adv. Catal.* **1979**, *28*, 2–78. (b) Ertl, G. *Adv. Catal.* **2000**, *45*, 1–69.
- (25) Reutt-Robey, J. E.; Doren, D. J.; Chabal, Y. J.; Christman, S. B. *J. Chem. Phys.* **1990**, *93*, 9113–9129.
- (26) Luo, J. S.; Tobin, R. G.; Lambert, D. K.; Fisher, G. B.; DiMaggio, C. L. *Surf. Sci.* **1992**, *274*, 53–62.
- (27) Xu, J.; Henriksen, P.; Yates, J. T. *J. Chem. Phys.* **1992**, *97*, 5250–5252.
- (28) Xu, J.; Yates, J. T. *J. Chem. Phys.* **1993**, *99*, 725–732.
- (29) Yates, J. T. *J. Vac. Sci. Technol., A* **1995**, *13*, 1359–1367.
- (30) Lebedeva, N. P.; Koper, M. T. M.; Feliu, J. M.; van Santen, R. A. *J. Phys. Chem. B* **2002**, *106*, 12938–12947.
- (31) Lebedeva, N. P.; Koper, M. T. M.; Feliu, J. M.; van Santen, R. A. *J. Electroanal. Chem.* **2002**, *524–525*, 242–251.
- (32) Lebedeva, N. P.; Rodes, A.; Koper, M. T. M.; Feliu, J. M.; van Santen, R. A. *J. Phys. Chem. B* **2002**, *106*, 9863–9872.
- (33) Marković, N. M.; Ross, P. N. *Surf. Sci. Rep.* **2002**, *45*, 117–229.
- (34) (a) Severson, M. W.; Weaver, M. J. *Langmuir* **1998**, *14*, 5603–5611. (b) Pozniak, B.; Scherson, D. A. *J. Am. Chem. Soc.* **2004**, *126*, 14696–14697. (c) Chang, S.-C.; Weaver, M. J. *J. Chem. Phys.* **1990**, *92*, 4582–4594.
- (35) Plyasova, L. M.; Molina, I. Yu.; Gavrilov, A. N.; Cherepanova, S. V.; Cherstiouk, O. V.; Rudina, N. A.; Savinova, E. R.; Tsirlina, G. A. *Electrochim. Acta* **2006**, *51*, 4477.
- (36) Petukhov, A. V.; Akemann, W.; Friederich, K. A.; Stimming, U. *Surf. Sci.* **1998**, *402–404*, 182–186.
- (37) Korzeniewski, C.; Kardash, D. *J. Phys. Chem. B* **2001**, *105*, 8663–8671.
- (38) Love, B.; Lipkowski, J. In *Electrochemical Surface Science. Molecular Phenomena at Electrode Surfaces*; Soriaga, M. P., Ed.; ACS Symposium Series 378; American Chemical Society: Washington, DC, 1988; pp 484–495.
- (39) McCallum, C.; Pletcher, D. *J. Electroanal. Chem.* **1976**, *70*, 277–290.
- (40) Gustavsson, M.; Fredriksson, H.; Kasemo, B.; Jusys, Z.; Kaiser, J.; Jun, C.; Behm, R. J. *J. Electroanal. Chem.* **2004**, *568*, 371–377.
- (41) Kucernak, A. Private communication.

- (42) Santos, E.; Leiva, E. P. M.; Vielstich, W. *Electrochim. Acta* **1991**, 36, 555.
- (43) Bergelin, M.; Herrero, E.; Feliu, J. M.; Wasberg, M. *J. Electroanal. Chem.* **1999**, 467, 74–84.
- (44) Jiang, J.; Kucernak, A. *J. Electroanal. Chem.* **2003**, 543, 187–199.
- (45) Anderson, A. B.; Neshev, N. M. *J. Electrochem. Soc.* **2002**, 149, E383–E388.
- (46) Narayanasamy, J.; Anderson, A. B. *J. Electroanal. Chem.* **2003**, 554–555, 35–40.
- (47) Saravanan, C.; Dunietz, B. D.; Marković, N. M.; Somorjai, G. A.; Ross, P. N.; Head-Gordon, M. *J. Electroanal. Chem.* **2003**, 554–555, 459–465.
- (48) Shubina, T. E.; Hartnig, Ch.; Koper, M. T. M. *Phys. Chem. Chem. Phys.* **2004**, 6, 4215–4221.
- (49) Gilman, S. *J. Phys. Chem.* **1964**, 68, 70–80.
- (50) Cuesta, A.; Couto, A.; Rincón, A.; Pérez, M. C.; López-Cudero, A.; Gutiérrez, C. *J. Electroanal. Chem.* **2006**, 586, 184–195.
- (51) Zhu, Y.; Uchida, H.; Watanabe, M. *Langmuir* **1999**, 15, 8757–8764.
- (52) (a) Saravanan, C.; Koper, M. T. M.; Markovic, N. M.; Head-Gordon, M.; Ross, P. N. *Phys. Chem. Chem. Phys.* **2002**, 4, 2660–2666. (b) Housmans, T. H. M.; Koper, M. T. M. *Electrochem. Commun.* **2005**, 7, 581–588.
- (53) Romanowski, W. *Surf. Sci.* **1969**, 18, 373–388.
- (54) Marković, N. M.; Schmidt, T. J.; Grgur, B. N.; Gasteiger, H. A.; Behm, R. J.; Ross, P. N. *J. Phys. Chem. B* **1999**, 103, 8568–8577.
- (55) Kim, C. S.; Korzeniewski, C. *Anal. Chem.* **1997**, 69, 2349–2353.
- (56) Collins, D. M.; Spicer, W. E. *Surf. Sci.* **1977**, 69, 85–113.
- (57) Reutt-Robey, J. E.; Doren, J. D.; Chabal, Y. J.; Christman, S. B. *Phys. Rev. Lett.* **1988**, 61, 2778–2781.
- (58) (a) Gland, J. L. *Surf. Sci.* **1980**, 93, 487–514. (b) Winkler, A.; Guo, X.; Siddiqui, H. R.; Hagans, P. L.; Yates, J. T. *Surf. Sci.* **1988**, 201, 419–443. (c) Gambardella, P.; Šljivančanin, Z.; Hammer, B.; Blanc, M.; Kuhnke, K.; Kern, K. *Phys. Rev. Lett.* **2001**, 87, 056103.
- (59) Koper, M. T. M.; Lebedeva, N. P.; Hermse, C. G. M. *Faraday Discuss.* **2002**, 121, 301–311.
- (60) Gomer, R. *Rep. Prog. Phys.* **1990**, 53, 917–1002.
- (61) Poelsema, B.; Verheij, L. K.; Comsa, G. *Phys. Rev. Lett.* **1982**, 49, 1731–1735.
- (62) Feibelman, P. J.; Hammer, B.; Nørskov, J. K.; Wagner, F.; Scheffler, M.; Stumpf, R.; Watwe, R.; Dumesic, J. *J. Phys. Chem. B* **2001**, 105, 4018–4025.
- (63) (a) Ansermet, J. P. Ph.D. Thesis, University of Illinois, Urbana–Champaign, IL, 1985. (b) Becerra, L. R.; Klug, C. A.; Slichter, C. P.; Sinfelt, J. H. *J. Phys. Chem.* **1993**, 97, 12014–12019.
- (64) Kobayashi, T.; Babu, P. K.; Gancs, L.; Chung, J. H.; Oldfield, E.; Wieckowski, A. *J. Am. Chem. Soc.* **2005**, 127, 14164.
- (65) Herrero, E.; Feliu, J. M.; Blais, S.; Radovic-Hrapovic, Z.; Jerkiewicz, G. *Langmuir* **2000**, 16, 4779.
- (66) Bewick, A.; Fleischmann, M.; Thirsk, H. R. *Trans. Faraday Soc.* **1962**, 58, 2200–2216.
- (67) Petukhov, A. V. *Chem. Phys. Lett.* **1997**, 277, 539–544.
- (68) Koper, M. T. M.; Jansen, A. P. J.; van Santen, R. A.; Lukkien, J. J.; Hilbers, P. A. J. *J. Chem. Phys.* **1998**, 109, 6051–6062.
- (69) Zhdanov, V. P.; Kasemo, B. *Surf. Sci.* **2003**, 545, 109–121.
- (70) Watanabe, M.; Motoo, S. *J. Electroanal. Chem.* **1975**, 60, 267–273.
- (71) Koper, M. T. M.; Lukkien, J. J.; Jansen, A. P. J.; van Santen, R. A. *J. Chem. Phys. B* **1999**, 103, 5522–5529.
- (72) Zhdanov, V. P.; Kasemo, B. *Surf. Sci. Rep.* **2000**, 39, 25–104.
- (73) Dunietz, B. D.; Marković, N. M.; Ross, P. N.; Head-Gordon, M. *J. Phys. Chem. B* **2004**, 108, 9888–9892.
- (74) Andreaus, B.; Eikerling, M. *J. Electroanal. Chem.*, submitted for publication.
- (75) Binder, K. In *Monte Carlo Methods in Statistical Physics*; Binder, K., Ed.; Topics in Current Physics 7; Springer: Berlin, Germany, 1986.
- (76) (a) Gillespie, D. T. *J. Comput. Phys.* **1976**, 22, 403–434. (b) Jansen, A. P. J. *Comput. Phys. Commun.* **1995**, 86, 1–12.
- (77) Haus, J. W.; Kehr, K. W. *Phys. Rep.* **1987**, 150, 263–406.
- (78) Park, S.; Wasileski, S. A.; Weaver, M. J. *J. Phys. Chem. B* **2001**, 105, 9719–9725.
- (79) (a) Strasser, P.; Eiswirth, M.; Ertl, G. *J. Chem. Phys.* **1997**, 107, 991–1003. (b) Zhang, J.; Datta, R. *J. Electrochem. Soc.* **2002**, 149, A1423–A1431. (c) Koper, M. T. M.; Schmidt, T. J.; Markovic, N. M.; Ross, P. N. *J. Phys. Chem. B* **2001**, 105, 8381–8386. (d) Bonnefont, A.; Varela, H.; Krischer, K. *ChemPhysChem* **2003**, 4, 1260–1263.
- (80) Zhdanov, V. P. *Surf. Sci. Rep.* **2002**, 45, 231–326.